Microchimica Acta (2022) 189: 11
https://doi.org/10.1007/s00604-021-05110-7

ORIGINAL PAPER

Complete experimental and theoretical characterization of nonlinear concentration gradient generator microfluidic device for analytical purposes

Paulo Henrique Maciel Buzzetti[1,2] · Maiara Mitiko Taniguchi[1] · Nayara de Souza Mendes[1] · Renata Corrêa Vicentino[3] · Jean Halison de Oliveira[1] · Bento Pereira Cabral Júnior[1] · Marcos de Souza[3] · Johny Paulo Monteiro[4] · Emerson Marcelo Girotto[1]

Received: 31 August 2021 / Accepted: 14 November 2021 / Published online: 6 December 2021
© The Author(s), under exclusive licence to Springer-Verlag GmbH Austria, part of Springer Nature 2021

Abstract

Microfluidic devices that generate stable concentration gradients are efficient instruments for automated calibration for analytical and bioanalytical systems. However, little attention has been paid to the development of reusable microfluidic concentration gradient generators, which can be useful for a range of species through mathematical characterization. In this work, we develop a microfluidic device based on three steps of serial dilution that were able to generate nonlinear concentration gradient for dyes and biomolecules. The microfluidic device was described mathematically, statistically and was suitable for reusable analytical and bioanalytical analysis. The device reproducibility was assessed by experimental tests, which have shown the same gradient concentration profile for different dyes and statistical reproducibility with 95% confidence interval for bovine serum albumin (BSA). Moreover, the experimental data converged well with those obtained by computational fluid dynamics simulation. Applicability was verified by coupling the microfluidic device to a surface plasmon resonance (SPR) biosensor, based on nanohole arrays with sensitivity of 358.7 nm RIU^{-1} determined by white-light SPR excitation exposed to different D-(+)-glucose aqueous solutions with 1.3361–1.4035 refractive index interval. The transmission light intensities obtained by the array of images allowed to quantify a pseudo-unknown BSA sample (160 μg mL^{-1}) at 138 μg mL^{-1}. The SPR analysis has been validated in parallel by fluorescence emissions, which showed a concentration of 154.8 ± 16.6 μg mL^{-1}.

Keywords Microfluidic devices · Automated calibration · Gradient generator · Optical biosensor · SPR · Nanohole arrays

Introduction

Microfluidic concentration gradient generators (MCGG) are systems that allow the generation of several concentrations through the division and combination of a fluid flow to dilute a concentrated fluid in a solvent one. Due to its miniaturized dimensions, MCGG are automatic, rapid, and portable devices. In addition, the systems require low fluid volume, which is according to green chemistry. These features agree with the point-of-care (POC) approach and can be integrated into multiple laboratory processes in lab-on-a-chip analytical systems [1, 2]. Dilution networks have also been reported for analytical purposes in several biological applications such as cell culture [3], chemotaxis [4], bacteria chemotaxis [5], cytotoxicity [6], biosensors [7], and others [8, 9].

In more recent examples, microfluidic devices have been applied in antibiotic susceptibility testing of bacteria. Sun et al. developed a gradient microfluidic chip integrated with a fluorescence detection platform for testing antibiotic resistance of *Salmonella* to ofloxacin and ampicillin [10]. Shi et al. also developed a concentration gradient generation platform for an antimicrobial susceptibility test to study the bacteriostasis using *Escherichia coli* to multiple

✉ Emerson Marcelo Girotto
emgirotto@uem.br

1 Materials Chemistry and Sensors Laboratories (LMSEN), Department of Chemistry, State University of Maringá, Colombo 5790, Maringá, PR 87020-900, Brazil

2 Present Address: DCM, CNRS, UMR 5250, Univ. Grenoble Alpes, F-38000 Grenoble, France

3 Department of Chemical Engineering, State University of Maringá, Colombo 5790, Maringá, PR 87020-900, Brazil

4 Department of Chemistry, Federal University of Technologic - Paraná, Marcílio Dias 635, Apucarana, PR 86812-460, Brazil

concentrations of an antibacterial drug (ceftizoxime) [11]. Its potential for chemotaxis applications was also confirmed and the proposed concentration generator platform could be utilized to conduct rapid drug screening and chemotaxis for clinical or experimental research at a cellular level. Tang et al. developed a hydroxyapatite-PDMS microfluidic chip to provide a highly bionic bone environment for bone-related cell culture and drug screening [12]. The concentration gradient of the drug doxorubicin hydrochloride model was successfully generated on a Christmas tree structure. Ganguly et al. developed a microfluidic hydrodynamic single-cell trapping and culturing platform of host-viral interactions that reported the influenza A virus interactions analysis under the gradient concentration of bafilomycin A1 treatment [13]. This facilitated the biological analysis and experimentation of virus infection into host cells. The main characteristics of microfluidic devices, as presented above, are summarized in Table S1.

The concentration gradient generators versatility is demonstrated through a series of examples with increasing complexity. However, an ideal concentration gradient generator should be able to reliably reproduce the same concentration gradient for any chemical species, thus dispensing recurrent calibrations process. This can be delimited if the mathematical description of the experimental gradient profile is defined to establish the concentration gradient of the generator application range. Nevertheless, it is still a challenge to achieve a controlled and reproducible concentration gradient, making many systems unsuitable for analytical purposes. Furthermore, fluid mixing and transport processes are complex, and the variety of chemical species is extensive. If we cannot generate concentration gradients for all existing species with a single device, it is possible to develop a device that is able to reproduce the same concentration gradient for a range of species from a mathematical description of the concentration gradient profile. This can be guaranteed from experimental and statistical analysis, which makes this system reusable. Furthermore, it does not need recurrent calibrations, it is attachable to any analytical systems, it is suitable for decentralized assays, and it is used as calibration standards.

Proposing a new concentration gradient generator device is not an easy task. Intuitively, the simplicity of a serial dilution steps for a microfluidic device may lead to a misinterpretation of the final concentration gradient. Wang et al. summarize various methods such as tree-shape, altered tree-shape, Y-shape, pressure balance, among other concentration gradient generation methods based on microfluidic systems [14]. An efficient way to estimate the serial dilution process can be accomplished by Hagen-Poiseuille's law $Q = \Delta P/R_H$, where Q, ΔP, and R_H are volumetric flow rate, pressure drop, and hydraulic resistance in a microfluidic channel, respectively [1]. The hydraulic resistance can be written as $R_H = C_{geometry}\,\mu(L/w^2h^2)$, where $C_{geometry}$ is the channel geometric coefficient, μ is the fluid viscosity, and L, w, and h are channel length, width, and height, respectively. As $R_H \propto L/w^2h^2$, then Q can be changed not only by injection pump (ΔP), but also by manipulating channel geometric parameters (L, w, and h) [15]. Thus, from the combined volumetric ratio between two fluids, it is possible to manipulate any dilution configuration. Some serial dilution systems of N steps are classified according to the volumetric flow ratios at the combination point: 10-fold log and 2-fold log, when the volumetric mixing ratios are 9:1 and 1:1 for all steps, respectively; linear, where the ratio changes for each dilution step 1:1, 1:2, 1:3, 1:4,... 1:N; Gaussian, among others [1, 16].

Interesting applications of MCGG have been found in the sensory platforms' development. The coupling of gradient generator devices to biosensors has already been explored and has proved to be an interesting alternative for reducing the reagents consumption and automating the mixture's handling. These devices have been coupled to sensors based on the surface plasmon resonance (SPR), which were the focus of current research [17]. The SPR phenomena are especially attractive for sensing because they are more sensitive than other techniques and can be developed in miniaturized systems [18].

In this way, we propose a symmetric MCGG with three serial dilution steps to create a nonlinear and reproducible concentration gradient for dyes and bovine serum albumin (BSA). An important point is that the gradient profile was extensively characterized and validated so that the applicability of the MCGG device was well determined. The MCGG was coupled with a nanohole arrays-based SPR biosensor for biomolecular quantification to test the performance of the dilution chip. This coupling enabled the calibration curve and the protein detection to be performed at the same time ("online detection"). A new aspect is that the MCGG works independently of the sensory platform to which it was attached. Thus, the MCGG chip proposed here could be used with several analytical systems through simple coupling adjustments.

Experimental

Nonlinear concentration gradient generator

The proposed microfluidic gradient generator (2x5-Y) device can be seen in Fig. 1a. It shows two inlets (A and B), five outlets (1, 2, 3, 4, and 5), "combiners," and "splitters" with a "Y" shape (Fig. 1b). The microfluidic device has three dilution steps composed of channels with rectangular cross section of 150 μm width, 100 μm height, and 50000 μm total length of the serpentine path. The microfluidic devices were fabricated in polydimethylsiloxane (PDMS) by soft lithography, which is reported in the supplementary material. The

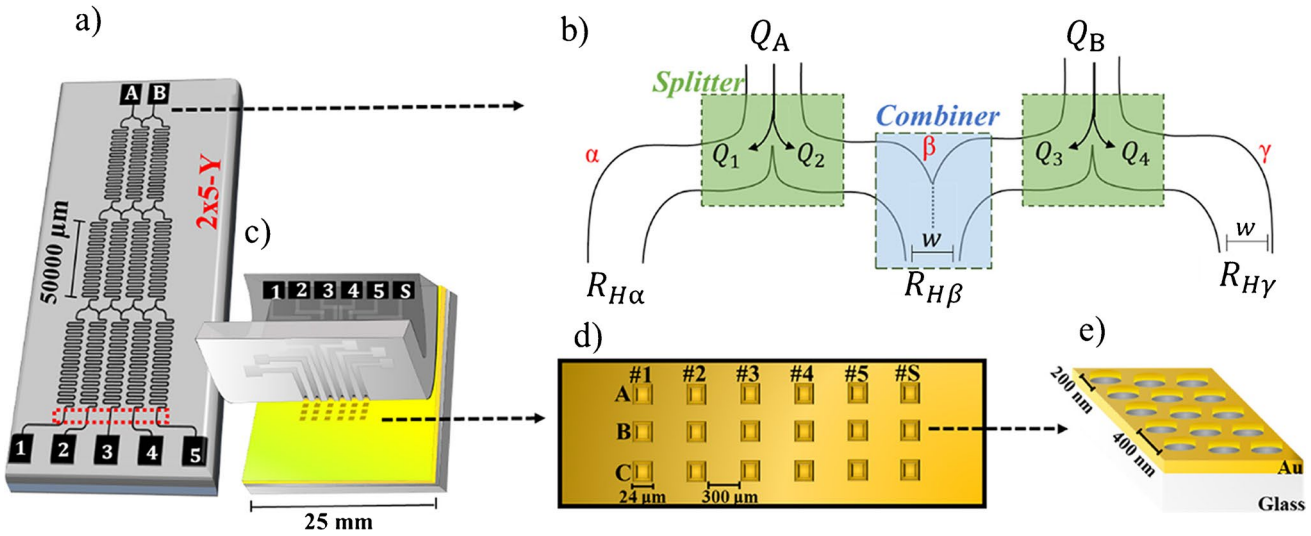

Fig. 1 Microfluidic gradient generator device, 2x5-Y; the dashed rectangle shows the region where the fluorescence images were assessed (**a**). Generic flows scheme of splitter (green square) and combiner (blue square) system (**b**). SPR biosensor based on nanohole arrays containing a matrix of 3 × 6 square arrays covered by PDMS piece with straight microchannels (SPR detection module) (**c**). An illustrative scheme of the 3 × 6 square arrays (**d**). Nanoholes configurations and dimensions of each array (**e**)

concentration gradients, as well as the complete cross-sectional channels homogeneity, were assessed by fluorescence images (fluorescence microscope TNI-06T-PL) using a 4× objective lens. For this, fluorescein solution (1.0 mmol L^{-1}, diffusivity $D_{fluor.} = 5.0 \times 10^{-10}$ m^2 s^{-1}, 95% Sigma Aldrich) and water were added to the inlets A and B, respectively, at $Q_A = Q_B = 1.000$ mL h^{-1}. Then, fluorescence images were obtained after the third dilution step (see the dashed rectangle in Fig. 1a). All images were processed using the ImageJ® software to collect the fluorescence intensity, which was used to estimate the gradient concentration formation.

The concentration gradients at the outlets were also evaluated using dyes and BSA. Rose bengal solution (10 µg mL^{-1}, $D_{rose.beng.} = 4.8 \times 10^{-10}$ m^2 s^{-1}, 95% Sigma Aldrich) and water were injected in the inlets at $Q_A = Q_B = 1.000$ mL h^{-1}. The dye concentrations were obtained using UV-Vis spectrophotometer (Ocean Optics, USB2000) by calibration curve obtention, considering the maximum absorption measurements at the 549 nm for aliquots collected at the outlets. Methylene blue solutions (10 µg mL^{-1}, $D_{blue.met.} = 8.3 \times 10^{-10}$ m^2 s^{-1}, ≥95% Sigma Aldrich) and water were used under different volumetric flow rates: $Q_A = Q_B = 0.800$, 1.000, and 1.200 mL h^{-1}. The maximum absorptions were monitored at 658 nm for the calibration curve obtention and dye quantification. Lastly, BSA solutions (300 µg mL^{-1} in phosphate buffer solution (PBS), $D_{BSA} = 5.9 \times 10^{-11}$ m^2 s^{-1}, Sigma Aldrich) and phosphate buffer saline (PBS, pH 7.45) were also injected at different volumetric flows: $Q_A = Q_B = 0.125$, 0.800, and 1.000 mL h^{-1}. Fluorescence emissions were monitored at 350 nm by excitation at 295 nm using a spectrofluorometer (Varian, Cary-Eclipse). Calibration curves were also performed to obtain BSA concentrations in the outlets.

Computational simulation

Computer simulations were performed to assess the theoretical concentration gradient. For this, the 2x5-Y device has been properly designed using AutoCAD 3D and performed on COMSOL Multiphysics® by computational fluid dynamics (CFD) module. The parameters used were as follows: BSA solution concentration, water dynamic viscosity, and density (at 25 °C) were defined as 300 µg mL^{-1}, 1.0020 × 10^{-3} Pa s, and 997 kg m^{-3}, respectively, and $Q_A = Q_B = 0.125$ mL h^{-1} [19].

The CFD module uses Navier-Stokes equation (Eq. 1) to describe the momentum conservation principle for laminar flow; diluted species transport model for mass conservation in incompressible systems (Eq. 2); and Fick's law (Eq. 3) for the diffusive and convective mass flow combination [20].

$$\rho\left(\frac{\partial u}{\partial t} + u \bullet \nabla u\right) = -\nabla p + \nabla \bullet \left(\mu\left(\nabla u + (\nabla u)^T\right) - \frac{2}{3}\mu(\nabla \bullet u)\mathrm{I}\right) + F \quad (1)$$

$$\frac{\partial C_A}{\partial t} = -\left(\nabla \bullet N_A\right) + R_A \quad (2)$$

$$N_{Az} = -cD_{AB}\frac{\partial x_A}{\partial z} + x_A\left(N_{Az} + N_{Bz}\right) \quad (3)$$

where: ρ—specific mass; u—fluid velocity; p—pressure; μ—viscosity; F—external forces; C_A—concentration of solute A; c—density; D_{AB}—diffusivity of molecule A in molecule

B; N_A and N_B—mass flows of molecules A and B in the flow direction; and x_A—molar fraction of molecule A.

Nanohole array confection and optical characterization

A matrix of 3 × 6 square arrays composed of 60 × 60 identical circular nanoholes (SPR platform) confectioned by a focused ion beam is reported in the supplementary material. A PDMS piece containing six straight microchannels was coupled to the SPR platform to allow the solutions flow over the arrays (Fig. 1c). This combination was called "SPR detection module" and it has five inlets for the flows that come from the 2x5-Y device and a sixth inlet for an independent injection of the sample. Arrays images obtained by scanning electron microscopy (SEM, Shimadzu Superscan SSX-550) were used to characterize the arrays and holes by Image-Pro Plus®.

The optical transmission, which is characteristic of the nanohole arrays, was carried according to the scheme in Fig. S1. Briefly, a white light beam (halogen lamp, 250 W) was collimated by a microscope (Quimis, Q738MIT) equipped with objective lens (50×) towards one nanohole array at a time. The SPR platform was positioned on an xyz table and exposed to a 1.3327 refractive index (milli-Q water, 25 °C). The extraordinary optical transmission (EOT) assigned to the SPR modes on each nanohole array was collected by an optical fiber connected to an UV-Vis spectrophotometer [21–24]. Afterwards, each nanohole array was individually exposed to different D-(+)-glucose aqueous solutions with 1.3361–1.4035 refractive index interval. Transmission spectra were recorded and the SPR platform sensitivity (nm RIU^{-1}) was determined by correlating the EOT vs. refractive index.

Surface plasmon resonance biosensor by image acquisition

Experimental setup (Fig. S2) to monitor the transmitted light intensity through the arrays by image acquisition using a charge-coupled device (CCD) camera was already reported by our group and it is shown in the supplementary material [25, 26]. The 2x5-Y device was combined with the SPR detection module as shown in Fig. S2. The concentration gradient (minor for major concentration) was coupled to the nanohole array sets #1, #2, #3, #4, and #5, respectively. The last nanohole arrays set, the #S (see Fig. 1d), was separated for sample detection. The combined system was used to detect BSA as a protein model. For this, BSA molecules were immobilized on the nanohole arrays. First, milli-Q water was injected, being $Q_A = Q_B = Q_S = 1.000$ mL h^{-1} for 30 min. Then, the flow stopped for 30 min (flow stabilization) and 75 images were collected. In sequence, 11-mercaptoundecanoic acid ethanolic solution (MUA; 0.50 mmol L^{-1}, 98 %, Sigma-Aldrich) was injected at $Q_A = Q_B = Q_S = 0.500$ mL h^{-1} for 6 h; after, an aqueous mixture of ethyl-3-(3-dimethylaminopropyl) carbodiimide hydrochloride (EDC; 0.1 mol L^{-1}, 98 %, Sigma-Aldrich) and N-hydroxysuccinimide (NHS; 0.1 mol L^{-1}, 98 %, Sigma-Aldrich) at $Q_A = Q_B = Q_S = 0.500$ mL h^{-1} was injected for 4 h. Finally, BSA (300 µg mL^{-1}) in PBS (pH 7.45) was injected to inlet A and only PBS to inlet B, while in inlet S a "pseudo-unknown" BSA solution at 160 µg mL^{-1} was injected. The injection process took place for 40 h at $Q_A = Q_B = Q_S = 0.125$ mL h^{-1}. After this, the flow stopped for 30 min and EOT images were recorded. All images were processed using the ImageJ® software to collect the average intensity of the transmitted light, considering the whole area of each nanohole array [27].

Results and discussion

Mathematic model, computational simulation, and experimental serial dilution

A serial gradient generator can be better understood by observing a generic scheme (Fig. 1b) of two splitters (green square) and one combiner (blue square). The volumetric flows division of inlet (Q_A and Q_B) are dependent on the hydraulic resistances that surround them, $R_{H\alpha}$, $R_{H\beta}$, and $R_{H\gamma}$ [1]. Obviously, the initial volumetric flow fraction assigned to each channel will influence its final concentration. Hydraulic resistance for a rectangular section channel can be determined by Eq. 4 [28]. If the channel length and width are identical for the channels α, β, and γ, it is expected that both will have the same hydraulic resistance. However, the β channel combines Q_2 and a Q_3 fractions, which come from Q_A and Q_B, respectively. The first consequence is that Q_2 and Q_3 face greater hydraulic resistance ($R_{H\beta} = 2.6 \times 10^{12}$ Pa s m^{-3}) than Q_1 and Q_4 ($R_{H\alpha} = R_{H\gamma} = 6.8 \times 10^{11}$ Pa s m^{-3}). Then, $R_{H\alpha} = R_{H\gamma}$ are ≈ 3.8 times smaller than $R_{H\beta}$ and, because this, $Q_1 = 4/5Q_A$ and $Q_2 = 1/5Q_A$. Similarly, $Q_3 = 1/5Q_B$ and $Q_4 = 4/5Q_B$. By extending this same process for the two other dilution steps of the 2x5-Y device, the final concentrations fractions in the five outlets are 0.00, 0.16, 0.50, 0.83, and 1.00. Note that a nonlinear profile is observed, and these coefficients describe a logistic sigmoidal curve given by $Y = a/(1 + e^{-k(X - x0)})$, where X is the output channels, Y is the measured intensity or concentration, a is the maximum magnitude of the measured intensity or concentration, k is the curve angular coefficient in the central part, and x_0 is the point at which $X = a/2$.

$$R_H = \frac{12\mu L}{wh^3\left(1 - \frac{h}{w}\left(\frac{192}{\pi^5}\sum_{n=1,3,5}^{\infty}\frac{1}{n^5}tanh\left(\frac{n\pi w}{2h}\right)\right)\right.} \quad (4)$$

To mathematically estimate the concentration fractions, it is necessary to assume that the serpentine length is sufficient for complete binary mixing. To experimentally assess this, a fluorescein solution was injected into the system. The collected fluorescence image (Fig. 2a) shows that at the end of the dilution process there is a fluorescence homogeneity along the channel width for the five output channels (see Fig. 2b, inset). This indicates that the length of the channel was sufficient to occur the complete fluids mixture along the channel path. Furthermore, it was observed the formation of identical concentration gradient to the mathematically estimated (Fig. 2b).

The concentration gradients were also monitored using rose bengal at 10 μg mL^{-1}. Again, the experimental behavior was similar to the one predicted mathematically (Fig. 2c). For methylene blue at 10 μg mL^{-1}, it was tested at different volumetric flows $Q_A = Q_B = 0.800$, 1.000, and 1.200 mL h^{-1}. The gradient experimentally obtained was similar to the mathematical one for all volumetric flows assessed (Fig. 2d). The inset in Fig. 2d shows the color gradient (related to a concentration gradient) formed over the dilution steps at $Q_A = Q_B = 1.200$ mL h^{-1}. This indicates that the 2x5-Y device has the ability to generate the same concentration gradient for the dye, independent of the input volumetric flow, as long as it is between the evaluated range (0.800 to 1.200 mL h^{-1}). Nevertheless, some molecules (proteins or biomolecules with higher molar mass or lower diffusivity) need longer serpentine lengths or reduction of the injection rate to complete the diffusion/convection mixture. Fig. 2e shows that when the BSA solution was injected at $Q_A = Q_B = 0.800$ and 1.000 mL h^{-1} there is no match between experimentally obtained and mathematical estimated concentration gradient. This is probably due to the serpentine length, which is insufficient to complete the mixing under these conditions. However, a reduction in the injection rate for $Q_A = Q_B = 0.125$ mL h^{-1} was sufficient to make the BSA concentration gradient statistically equal to the mathematically estimated one.

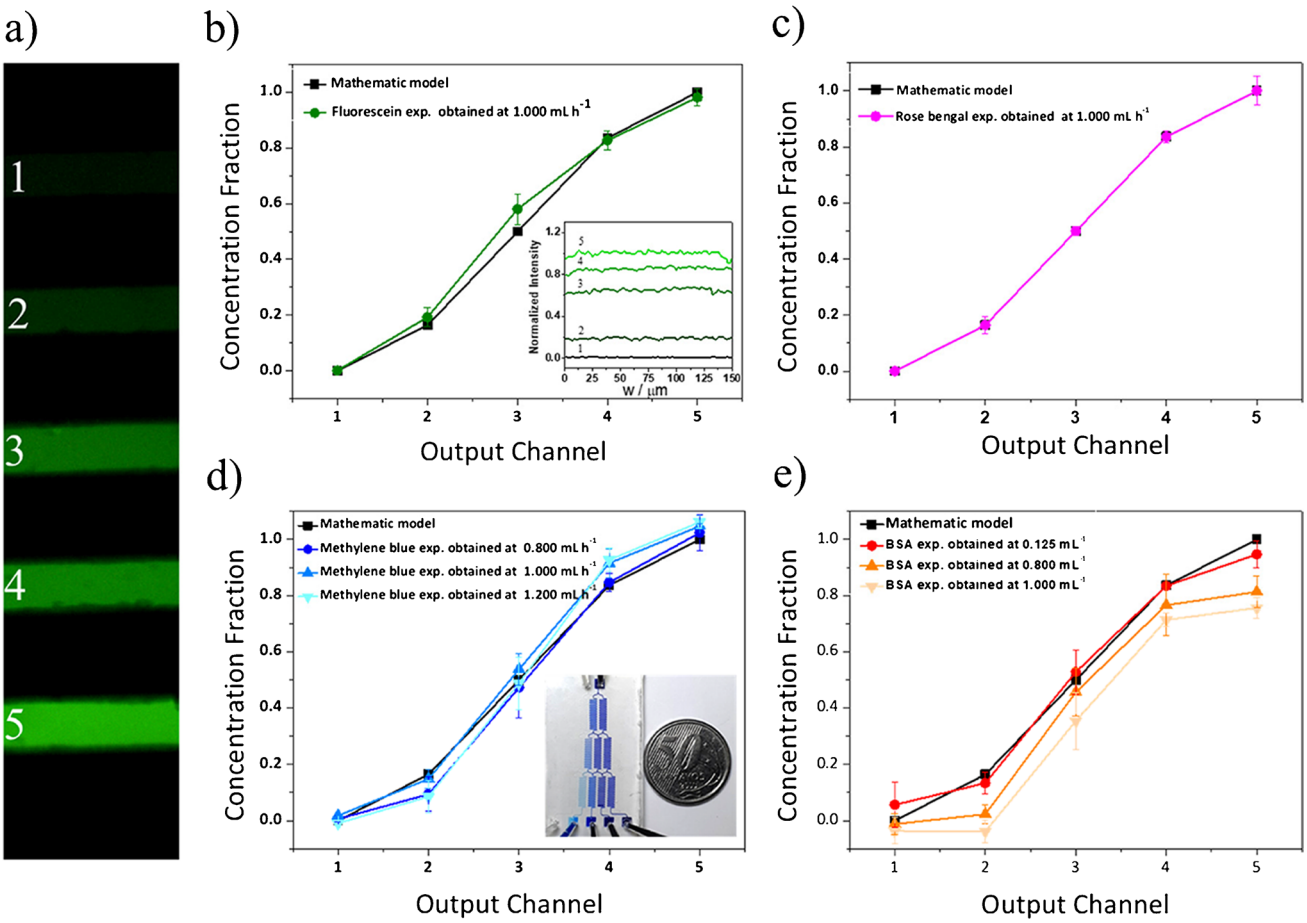

Fig. 2 Fluorescence image of the 2x5-Y device at the end dilution process for the fluorescein solution (**a**). Concentration fraction for the 2x5-Y at the end dilution process obtained mathematically and by fluorescein fluorescence intensity measurements (the inset shows normalized fluorescence intensity at some points along the channels width) (**b**), by rose bengal visible absorption (**c**), methylene blue visible absorption at different volumetric flows (the inset shows the visual color gradient obtention) (**d**), and BSA fluorescence emission at different volumetric flows (**e**)

In microfluidic systems, the characteristic flow and the binary mixtures are discussed from Reynolds and Péclet numbers, respectively [21]. While the Reynolds number ($R_e = c\nu D_h/\mu$) expresses the ratio of inertial forces to the viscous forces, the Péclet number ($P_e = uD_h/D$) expresses the importance of the convective process to the diffusive process in binary mixtures [29], where c is the fluid density, u is flow velocity, D_h is the hydraulic diameter ($D_h = 4A/S$), S perimeter of the channel, A is the sectional area, and D is the diffusivity of the solute. For the injection rates used in this work, the Reynolds numbers range from 0.23 to 2.21, being characterized as laminar flow [30]. On the other hand, the Péclet number applied to fluorescein, methylene blue, rose bengal, and BSA solutes indicates values that range from 0.33×10^3 to 45.18×10^3, which is characteristic of a predominantly convective mixing process [30]. The convection process must have aided in quickly mixing the fluids. This factor was responsible for achieving complete mixing, mainly for BSA, in the short microfluidic path used (50000 µm), even under a laminar flow.

Fig. 3a displays the computational simulation of concentration fractions for the 2x5-Y device exposed to protein solution (BSA, 300 µg mL^{-1}) at $Q_A = Q_B = 0.125$ mL h^{-1}. The concentration fractions by CFD computational simulation and mathematic model are similar. Moreover, both are in agreement with the value experimentally obtained by BSA fluorescence emission. Considering the data convergence between the mathematic model, experimental, and computational simulation with their respective standard deviations summarized in Table 1, the concentration fractions can be efficiently predicted mathematically and by computer simulation, as long as the mixing process is ideally satisfied. In addition, this also demonstrates that the device construction by soft lithography is efficient and can adequately reproduce the projected design for the microchannels system. Lastly, a statistical reproducibility with a 95% confidence interval curve was performed with the experimentally obtained data for the BSA. Fig. 3b displays a narrow confidence range for the dilution coefficients, considering any experimental analysis performed on the 2x5-Y device with BSA or any other solute with diffusivity greater than or equal to that of BSA at 0.125 mL h^{-1}.

Table 1 BSA concentration coefficients for the 2x5-Y device obtained by mathematic model, computational simulation, and fluorescence emission (experimental)

Output channel	Mathematic model	Computational simulation (0.125 mL h^{-1})	Fluorescence emission (0.125 mL h^{-1})
1	0.00	0.00 ± 0.00	0.05 ± 0.08
2	0.16	0.18 ± 0.02	0.13 ± 0.04
3	0.50	0.50 ± 0.04	0.53 ± 0.08
4	0.83	0.83 ± 0.02	0.83 ± 0.01
5	1.00	1.00 ± 0.00	0.95 ± 0.05

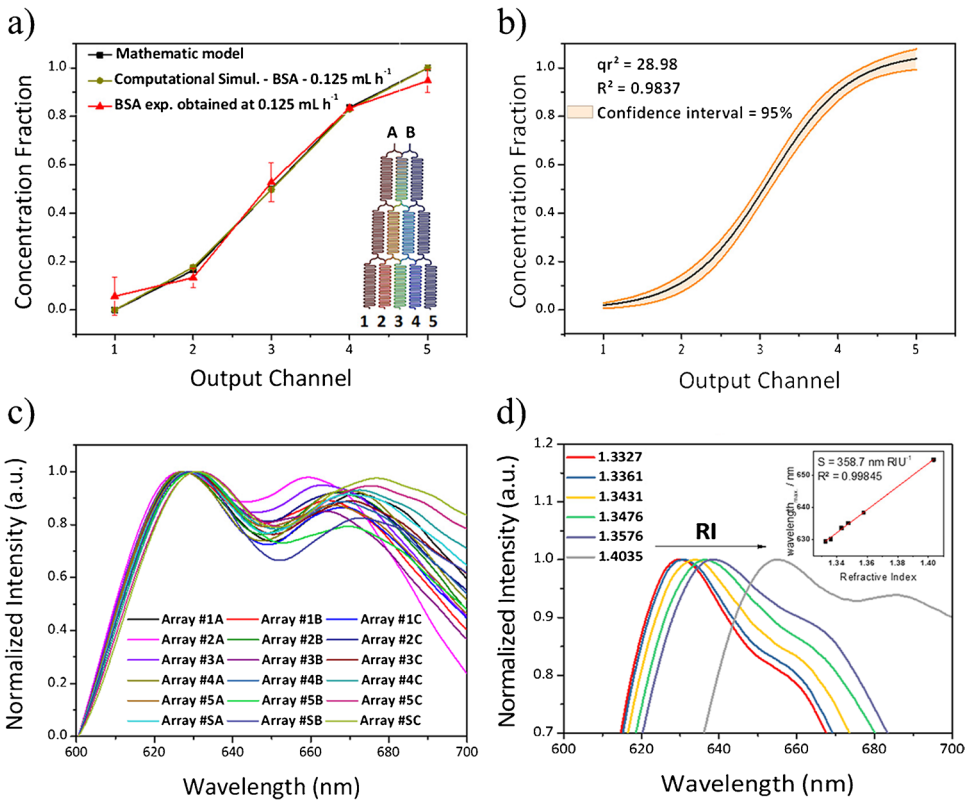

Fig. 3 Concentration fractions obtained mathematically by computational simulation on CFD software (the inset shows the obtained concentration gradient of 2x5-Y device by CFD simulation) and by BSA fluorescence emission (**a**). Concentration gradient reproducibility to 2x5-Y device with 95% confidence interval (**b**). EOT spectra of white light through for all nanohole arrays in water (**c**). SPR biosensor sensitivity obtained from the relationship between the maximum transmission redshift of the light to the refractive index for one nanohole array (**d**)

For practical proposes, it is possible to ensure that any solute capable of homogenizing completely in 50000 µm serpentine path length will reproduce the same concentration coefficients.

Nanohole array characterization

EOT phenomenon is a greater intensity of transmitted light observed through nanohole arrays in metallic films [31]. The transmitted light is related to the surface plasmon resonance excitation that occurs on either side of the metal film [32]. The light waves are coupled with a metal conduction band as SPs on one side and transmitted for the other side [33]. The maximum wavelength (λ_{max}) of the transmitted light can be manipulated by refractive index variation and by the holes periodicity and geometry [23]. For the holes with 196.7 ± 5.3 nm diameter and 401.3 ± 4.7 nm periodicity (SEM image, Fig. S3), the SPs excitation can be performed using a He/Ne laser with emission at 632.8 nm [25]. Fig. 3c displays the transmission spectra obtained with white light for all nanohole arrays in water (n = 1.3327, 25 °C). It is evident that one of the transmission maximums occurs around 630 nm. This confirms that the He/Ne laser emission (at 632.8 nm) is compatible with the nanohole arrays transmission spectra. Fig. 3d shows transmission spectra of white light for one nanohole array under the different refractive index. The sensitivity $S = \Delta\lambda/\Delta n = \lambda(\varepsilon_m/n(n^2 + \varepsilon_m)) = 358.7$ nm RIU^{-1} with $R^2 = 0.9985$ (see Fig. 3d) was determined by correlating the light maximum transmission redshift to the refractive index for one nanohole array [22, 34]. The sensitivity curve highlights the great ability of the substrate to monitor refractive index variations [26]. This feature makes the substrate efficient for detecting molecules on the metal surface (sensor).

Surface plasmon resonance biosensor by image acquisition

The SPR biosensor was prepared for BSA immobilization on the MUA/EDC-NHS self-assembled monolayers. Fig. 4a shows the EOT intensity for the arrays sets from #1 to #5 and #S, before and after the BSA exposition. The EOT intensities were obtained from CCD images such as those exemplified in Figure 4a inset. In these images, it is notable that the transmitted light intensity through all the arrays decreases after BSA molecules immobilization. In addition, the curve in Figure 4a shows that the decrease in EOT average intensity was greater as the BSA concentration increased from #1 to #5. The greater amount of immobilized BSA molecules causes greater redshifts in the EOT bands. The redshift was accompanied by a decrease in the transmitted light intensity at a fixed wavelength of 632.8 nm [25]. The module of the EOT average intensity for the arrays sets from #1 to #5 was normalized and plotted as a function of each output channel (Fig. 4b). As expected,

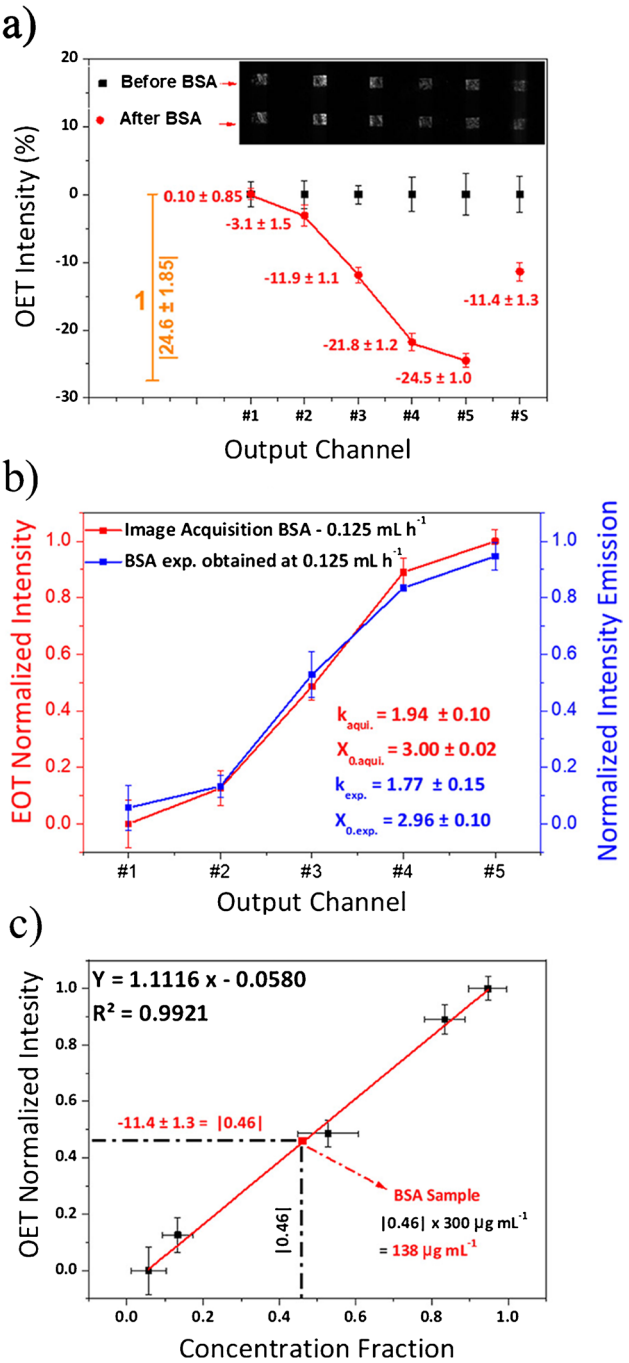

Fig. 4 EOT average intensity for the arrays from #1 to #5 and #S, before and after BSA exposition; the inset shows CCD images for some arrays before and after BSA exposition (**a**). Module of the EOT average normalized intensity assessed by the arrays images acquisition and BSA average normalized emission intensity for each channel (**b**). Calibration curve obtained by plot of the EOT average normalized intensity as a function of the concentration fraction (**c**)

the profile of the intensity decreasing module is a logistic curve equal to that obtained by BSA fluorescence emission. In addition, it was observed that the parameters k and x_0 of the logistic curve equation are statistically equal for both

response types (Fig. 4b). This confirms that the number of molecules immobilized on the arrays was proportional to the BSA concentration in the solution. The concentration fractions of each channel (obtained by BSA emission intensity, see Fig. 3a) were plotted in function of EOT average normalized intensity to obtain the calibration curve shown in Fig. 4c. A direct and linear response was observed showing $R^2 = 0.9921$. From the observed response it was possible to verify that the pseudo-unknown BSA sample (nominal value was 160 μg mL^{-1}) caused an EOT average intensity of $-11.4 \pm 1.3\%$ with respect to one before the BSA exposition (see Fig. 4a for the #S array set). This represents 0.46 for the EOT average normalized intensity, which is equivalent to a 0.46 concentration fraction (by interpolation on the calibration curve). Considering that the initial BSA concentration applied to the 2x5-Y device was 300 μg mL^{-1}, this means that the sample BSA concentration corresponds to 138 μg mL^{-1}. Lastly, in order to validate the pseudo-unknown quantified concentration of BSA, the sample was also quantified by fluorescence emissions immediately thereafter the SPR analysis was carried out. The validated concentration was 154.8 ± 16.6 μg mL^{-1}. The value was statistically equal to the one determined by the images acquisition method.

Despite the gradient generator device versatility demonstrated through coupling to a nanohole arrays-based SPR biosensor, the association between a simple serial dilution with a splitter and combiner with "Y" shape may lead to a misinterpretation of the mathematical final concentration gradient. Moreover, the soft lithography technique used to fabricate the gradient generator device may impose difficulties to make defined channels, which are decisive factors for the hydraulic resistances and consequent to the combined volumetric ratio in binary mixing. In addition, these kinds of gradient generator devices are known for easy blocking and leakage.

Conclusions

The gradient generator device proposed in this work had a design with splitter and combiner with "Y" shape, three steps of serial dilution, and five independent outlet channels specially designed to be attachable to any analytical systems. These features enabled the generation and the reproduction with excellent accuracy of a nonlinear concentration gradient for different dyes and BSA. The experimental gradient profile was described mathematically and statistically; moreover, it is possible to state that it can be applied to any other solute with diffusivity greater than or equal to that of BSA if the maximum volumetric flow reported is respected. The applicability of the autonomous gradient concentration generator was verified as an online calibration curve to quantify a pseudo-unknown BSA sample by coupling it to a nanohole arrays-based SPR biosensor confectioned on a gold film, in order to monitor extraordinary optical transmission variation assigned to the SPR modes by image acquisition method. The coupled systems were satisfactorily efficient to detect and quantify the pseudo-unknown BSA sample with an accuracy of 89.1% in relation to the pseudo-unknown BSA concentration validated in parallel by fluorescence emission. Finally, the MCGG proposed here operates in a totally independent way, which enables its use in various analytical systems for building automatic curves. Furthermore, this concept can be extended to other complex analytes as virus, bacteria, and antibodies and to minimize errors caused by sample manipulation and interference from environmental fluctuations due to the time gap between obtaining the calibration curve and the quantification moment. Subsequently, the plasmonic biosensor coupled to the autonomous gradient generator device proposed here was an excellent example of the versatility of MCGG for biological analysis.

Supplementary Information The online version contains supplementary material available at https://doi.org/10.1007/s00604-021-05110-7.

Author contribution Conceptualization: Paulo Henrique Maciel Buzzetti, Maiara Mitiko Taniguchi, Bento Pereira Cabral Júnior, Jean Halison de Oliveira, and Johny Paulo Monteiro; data curation: Paulo Henrique Maciel Buzzetti, Nayara Pereira Mendes, Maiara Mitiko Taniguchi, and Bento Pereira Cabral Júnior; formal analysis: Paulo Henrique Maciel Buzzetti, Maiara Mitiko Taniguchi, Renata Corrêa Vicentino, and Jean Halison de Oliveira; investigation: Paulo Henrique Maciel Buzzetti, Maiara Mitiko Taniguchi, Bento Pereira Cabral Júnior, and Johny Paulo Monteiro; validation: Paulo Henrique Maciel Buzzetti and Johny Paulo Monteiro; writing original draft preparation: Paulo Henrique Maciel Buzzetti, Maiara Mitiko Taniguchi, and Renata Corrêa Vicentino; writing review and editing: Marcos de Souza, Johny Paulo Monteiro, and Emerson Marcelo Girotto; visualization: Paulo Henrique Maciel Buzzetti and Maiara Mitiko Taniguchi; supervision: Marcos de Souza, Johny Paulo Monteiro, and Emerson Marcelo Girotto; project administration: Johny Paulo Monteiro and Emerson Marcelo Girotto; funding acquisition: Marcos de Souza and Emerson Marcelo Girotto.

Funding This work was also supported by CNPq (Brazil) through Inomat-INCT, National Institute for Complex Functional Materials (CNPq 573644/2008-0) and by Brazilian Federal Agency for Support and Evaluation of Graduate Education (CAPES).

Availability of data and material The data that support the findings of this study are available with the corresponding author, Emerson Marcelo Girotto, upon reasonable request.

Code availability Not applicable.

Declarations

Ethics approval Not applicable.

Consent to participate Not applicable.

Consent for publication Not applicable.

Conflict of interest The authors declare no competing interests.

References

1. Lee K, Kim C, Ahn B et al (2009) Generalized serial dilution module for monotonic and arbitrary microfluidic gradient generators. Lab Chip 9:709–717. https://doi.org/10.1039/b813582g
2. Hu C, Liu J, Chen H, Nie F (2017) Microfluidic platforms for gradient generation and its applications. Biochem Anal Biochem 06:3–10. https://doi.org/10.4172/2161-1009.1000320
3. Ye N, Qin J, Shi W et al (2007) Cell-based high content screening using an integrated microfluidic device. Lab Chip 7:1696–1704. https://doi.org/10.1039/b711513j
4. Kim D, Haynes CL (2012) Neutrophil chemotaxis within a competing gradient of chemoattractants. Anal Chem 84:6070–6078. https://doi.org/10.1021/ac3009548
5. Ge A, Hu L, Wang X et al (2018) Logarithmic bacterial gradient chip for analyzing the effects of dietary restriction on C. elegans growth. Sensors Actuators, B Chem 255:735–744. https://doi.org/10.1016/j.snb.2017.08.088
6. Pasirayi G, Scott SM, Islam M et al (2014) Low cost microfluidic cell culture array using normally closed valves for cytotoxicity assay. Talanta 129:491–498. https://doi.org/10.1016/j.talanta.2014.06.020
7. Yan S, Chu F, Zhang H et al (2019) Rapid, one-step preparation of SERS substrate in microfluidic channel for detection of molecules and heavy metal ions. Spectrochim Acta - Part A Mol Biomol Spectrosc 220:117113. https://doi.org/10.1016/j.saa.2019.05.018
8. Lee B, Jin SH, Noh YM et al (2018) Scalable static droplet array for biochemical assays based on concentration gradients. Sensors Actuators, B Chem 273:1572–1578. https://doi.org/10.1016/j.snb.2018.07.076
9. Chen X, Ji B, Gao X et al (2020) High-throughput generation of a concentration gradient on open arrays by serial and parallel dilution for drug testing and screening. Sensors Actuators, B Chem 305:127487. https://doi.org/10.1016/j.snb.2019.127487
10. Sun J, Ren Y, Ji J et al (2021) A novel concentration gradient microfluidic chip for high-throughput antibiotic susceptibility testing of bacteria. Anal Bioanal Chem 413:1127–1136. https://doi.org/10.1007/s00216-020-03076-8
11. Shi H, Hou Z, Zhao Y et al (2019) Rapid and steady concentration gradient generation platform for an antimicrobial susceptibility test. Chem Eng J 359:1327–1338. https://doi.org/10.1016/j.cej.2018.11.046
12. Tang Q, Li X, Lai C et al (2021) Bioactive materials fabrication of a hydroxyapatite-PDMS microfluidic chip for bone-related cell culture and drug screening. Bioact Mater 6:169–178. https://doi.org/10.1016/j.bioactmat.2020.07.016
13. Ganguly R, Lee B, Kang S et al (2021) Microfluidic single-cell trapping and cultivation for the analysis of host-viral interactions. Biotechnol Bioprocess Eng 26:179–187. https://doi.org/10.1007/s12257-020-0143-1
14. Wang X, Liu Z, Pang Y (2017) Concentration gradient generation methods based on microfluidic systems. RSC Adv 7:29966–29984. https://doi.org/10.1039/c7ra04494a
15. Jeon J, Choi N, Chen H et al (2019) SERS-based droplet microfluidics for high-throughput gradient analysis. Lab Chip 19:674–681. https://doi.org/10.1039/C8LC01180J
16. Zheng G, Lu L, Yang Y et al (2018) Development of microfluidic dilution network-based system for lab-on-a-chip microalgal bioassays. Anal Chem 90:13280–13289. https://doi.org/10.1021/acs.analchem.8b02597
17. Escobedo C, Chou YW, Rahman M et al (2013) Quantification of ovarian cancer markers with integrated microfluidic concentration gradient and imaging nanohole surface plasmon resonance. Analyst 138:1450–1458. https://doi.org/10.1039/c3an36616b
18. Escobedo C (2013) On-chip nanohole array based sensing: a review. Lab Chip 13:2445–2463. https://doi.org/10.1039/c3lc50107h
19. Oh KW, Lee K, Ahn B, Furlani EP (2012) Design of pressure-driven microfluidic networks using electric circuit analogy. Lab Chip 12:515–545. https://doi.org/10.1039/c2lc20799k
20. Bird RB, Stewart WE, Lightfoot EN (2006) Transport phenomena. Wiley, New York
21. Eftekhari F, Escobedo C, Ferreira J, Duan X, Girottoll EM, Brolo EG, Gordon R, Sinton D (2009) Nanoholes as nanochannels: flow-through plasmonic sensing. Anal Chem 81 (11):4308–4311. https://pubs.acs.org/doi/10.1021/ac900221y
22. Monteiro JP, de Oliveira JH, Radovanovic E et al (2016) Microfluidic plasmonic biosensor for breast cancer antigen detection. Plasmonics 11:45–51. https://doi.org/10.1007/s11468-015-0016-1
23. Monteiro JP, Carneiro LB, Rahman MM et al (2013) Effect of periodicity on the performance of surface plasmon resonance sensors based on subwavelength nanohole arrays. Sensors Actuators, B Chem 178:366–370. https://doi.org/10.1016/j.snb.2012.12.090
24. Monteiro JP, Ferreira J, Sabat RG et al (2012) SPR based biosensor using surface relief grating in transmission mode. Sensors Actuators, B Chem 174:270–273. https://doi.org/10.1016/j.snb.2012.08.026
25. Monteiro JP, Predabon SM, Bonafé EG et al (2017) SPR platform based on image acquisition for HER2 antigen detection. Nanotechnology 28:045206. https://doi.org/10.1088/1361-6528/28/4/045206
26. Predabon SM, Buzzetti PHM, Visentainer JEL, et al (2020) Detection of tumor necrosis factor-alpha cytokine from the blood serum of a rat infected with Pb18 by a gold nanohole array-based plasmonic biosensor. J Nanophotonics 14. https://doi.org/10.1117/1.JNP.14.036004
27. Johnsson B, Löfås S, Lindquist G (1991) Immobilization of proteins to a carboxymethyldextran-modified gold surface for biospecific interaction analysis in surface plasmon resonance sensors. Anal Biochem 198:268–277. https://doi.org/10.1016/0003-2697(91)90424-R
28. Cornish RJ (1928) Flow in a pipe of rectangular cross-section. Proc R Soc A Math Phys Eng Sci 120:691–700. https://doi.org/10.1098/rspa.1928.0175
29. Gobby D, Angeli P, Gavriilidis A (2001) Mixing characteristics of T-type microfluidic mixers. J Micromechanics Microengineering 11:126–132
30. Choban ER, Markoski LJ, Wieckowski A, Kenis PJA (2004) Microfluidic fuel cell based on laminar flow. J Power Sources 128:54–60. https://doi.org/10.1016/j.jpowsour.2003.11.052
31. Kamholz AE, Weigl BH, Finlayson BA, Yager P (1999) Quantitative analysis of molecular interaction in a microfluidic channel: the T-sensor. Anal Chem 71:5340–5347
32. Ebbesen TW, Lezec HJ, Ghaemi HF et al (1998) Extraordinary optical transmission through sub-wavelenght hole arrays. Nature 391:667–669. https://doi.org/10.1038/35570
33. Feng L, Dawson P (2007) Optical transmission through single subwavelength apertures using prism coupled input of laser light of annular intensity profile. Opt Express 15:17863. https://doi.org/10.1364/oe.15.017863
34. Genet C, Ebbesen TW (2009) Light in tiny holes. Nanosci Technol A Collect Rev from Nat Journals 445:205–212. https://doi.org/10.1142/9789814287005_0021

Publisher's note Springer Nature remains neutral with regard to jurisdictional claims in published maps and institutional affiliations.